Journal of Electrochemistry

Volume 25
Issue 1 *Special Issue of Next-Generation Secondary Batteries*

2019-02-28

Ni/Mn_3O_4/$NiMn_2O_4$ Double-Shelled Hollow Spheres Embedded into Reduced Graphene Oxide as Advanced Anodes for Sodium-Ion Batteries

Chong YAN

Hua-ri KOU

Bo YAN

Xiao-jing LIU

De-jun LI

Xi-fei LI
1. Tianjin International Joint Research Centre of Surface Technology for Energy Storage Materials, College of Physics and Materials Science, Tianjin Normal University, Tianjin 300387, China; 2. Institute of Advanced Electrochemical Energy & School of Materials Science and Engineering, Xi'an University of; Technology, Xi'an, Shanxi 710048, China, Xi'an University of Technology, Xi'an 710048, China;,
xfli2011@hotmail.com

Recommended Citation

Chong YAN, Hua-ri KOU, Bo YAN, Xiao-jing LIU, De-jun LI, Xi-fei LI. Ni/Mn_3O_4/$NiMn_2O_4$ Double-Shelled Hollow Spheres Embedded into Reduced Graphene Oxide as Advanced Anodes for Sodium-Ion Batteries[J]. *Journal of Electrochemistry*, 2019 , 25(1): 112-121.
DOI: 10.13208/j.electrochem.180546
Available at: https://jelectrochem.xmu.edu.cn/journal/vol25/iss1/9

DOI: 10.13208/j.electrochem.180546 **Artical ID**:1006-3471(2019)01-0112-10
Cite this: *J. Electrochem.* **2019**, *25*(1): 112-121 **Http**://electrochem.xmu.edu.cn

$Ni/Mn_3O_4/NiMn_2O_4$ Double-Shelled Hollow Spheres Embedded into Reduced Graphene Oxide as Advanced Anodes for Sodium-Ion Batteries

YAN Chong[1], KOU Hua-ri[2], YAN Bo[2], LIU Xiao-jing[1], LI De-jun[1], LI Xi-fei[1,2*]
(1. *Tianjin International Joint Research Centre of Surface Technology for Energy Storage Materials, College of Physics and Materials Science, Tianjin Normal University, Tianjin* 300387, *China*; 2. *Institute of Advanced Electrochemical Energy & School of Materials Science and Engineering, Xi'an University of Technology, Xi'an, Shanxi* 710048, *China*, *Xi'an University of Technology, Xi'an* 710048, *China*)

Abstract: Delicately building the unique nanocomposite with the combination of hollow structure and reduced graphene oxide (rGO) is highly desirable and still remains a great challenge in the field of energy conversion and storage. In this work, $Ni/Mn_3O_4/NiMn_2O_4$ double-shelled hollow spheres coated by rGO (denoted as R-NMN) have been successfully synthetized via one-step rapid solvothermal treatment followed by subsequent annealing for the first time. Served as anodes for sodium ion batteries (SIBs), the R-NMN composite containing 25wt% rGO exhibits a high discharge capacity of 187.8 $mAh\cdot g^{-1}$ after 100 cycles at 50 $mA\cdot g^{-1}$ in the potential range between 0.01 V and 3.0 V (vs. Na^+/Na). When cycled at different current densities of 100, 200, 400, and 800 $mA\cdot g^{-1}$, the nanocomposites deliver the reversible capacities of 213.45, 192.9, 171.7, and 149.9 $mAh\cdot g^{-1}$, respectively, indicating a satisfactory rate capability. Our conclusions reveal that the significant improvement in electrochemical performance is mainly attributed to the enhanced conductivity, reduced ion diffusion distance and suppressed volume fluctuation. The modification strategy proposed in this study can be extended to the design of other electrode materials for sodium storage and beyond.

Key words: $Ni/Mn_3O_4/NiMn_2O_4$; reduced graphene oxide; anode materials; sodium-ion batteries
CLC Number: O646 **Document Code**: A

As one of the dazzling energy storage devices, lithium ion batteries (LIBs) have attracted considerable attentions and been extensively studied in recent years due to their long cycling life, high energy density, great safety, and environmental friendliness [1-4]. However, lithium lack in resources as well as uneven distribution impedes the further applications and developments of LIBs[5]. Recently, sodium ion battery (SIB) has been regarded as a promising candidate to replace LIB for its acceptable energy/power density and the abundant of raw materials with low costs and wide distributions. In view of the large radius of Na^+ (1.02 Å) over the Li^+ radius (0.76 Å), unfortunately, SIBs often suffer from huge volume changes and sluggish reaction kinetics. Especially for the anode materials, it has been long considered as one of the most knotty components for typical graphitic carbons employed in LIBs barely intercalating sodium ions. Therefore, searching for alternative anode materials with superior performance is of vital importance to facilitate the practical application of SIBs[6-8].

Recently, researchers have witnessed that the binary transition-metal oxides (TMOs) show very promising applications in SIBs, in comparison to the single TMOs, originating from relatively high electronic conductivity and large reversible capacity[9-11]. Nevertheless, the electrochemical performance of pristine binary TMOs is still unsatisfactory due to the sluggish

Received: 2018-07-02, Revised: 2018-08-03 *Corresponding author, Tel: (86)13502042013, E-mail: xfli2011@hotmail.com

electronic/ionic transport and large volume effect. To conquer the inherent drawbacks of binary TMOs, one facile approach is to tailor the unique nanostructures, particularly for designing hollow structures or yolk-shell structures, which often manifests various attractive features to boost the high-efficiency energy storage including: (i) large electrode/electrolyte contact surface; (ii) shortening path length for electronic/ion transport; (iii) alleviating the volume variation[12-17]. For example, Chen et al.[18] reported the design and synthesis of hollow porous $NiCo_2O_4$-nanoboxes (NCO-NBs) with zeolitic imidazolate framework-67 nanocrystals as self-sacrificial template. The resulting NCO-NBs anode enhanced sodium storage with a high initial discharge capacity of 826 $mAh\cdot g^{-1}$ at a current density of 50 $mA\cdot g^{-1}$ and moderate capacity retention of 328 $mAh\cdot g^{-1}$ after 30 cycles, resulting from the as-prepared hierarchical nanoboxes with high specific surface area, promotional transports of ions and electrons, and improved structural stability.

Another effective approach for addressing the drawbacks is the masterly combination of TMOs with highly conductive matrixes, which can effectively improve the active material utilization and/or alleviate the volume effect. Up to now, various conductive matrixes have been widely explored, including amorphous carbon[19], ordered mesoporous carbon materials[20], carbon nanotubes[21], and graphene nanosheets[22-23], which have yielded very competitive performance in the storage of alkali metal ions. Among numerous conductive matrixes, rGO or graphene is preferable to replace other matrixes owing to its extraordinary properties including high electrical conductivity, unusual mechanical strength, and large specific surface area. For example, Cai et al.[24] reported the $CoMn_2O_4$ nanoparticles loaded onto rGO as anode materials for SIBs, which delivered a high discharge capacity of 114.0 $mAh\cdot g^{-1}$ after 60 cycles at a current density of 200 $mA\cdot g^{-1}$. Similarly, Zou et al.[25] synthesized the hierarchical NiO/Ni nanocrystals covered with graphene shells which also demonstrated promising performance as SIBs anode materials beneficial from the continuous conductive network and the buffered volume change. Obviously, using any of the aforementioned approaches can significantly improve the sodium storage of binary TMOs[26-30], but at this stage the majority of studies either focuses only on the design of unique nanostructured TMOs or employs an uncompetitive nanostructured texture to combine with rGO. Therefore, it is still a great desire to build a superior nanocomposite with the combination of hollow nanostructure and rGO for tackling the challenges facing TMOs.

In this study, rGO coated $Ni/Mn_3O_4/NiMn_2O_4$-(R-NMN) double-shelled hollow spheres were fabricated by one-step solvothermal treatment followed by subsequent annealing, here the existence of metal Ni can further enhance electrical conductivity. The effects of rGO content on the sodium storage of nanocomposites were systematically investigated. The resulting nanocomposite anodes have demonstrated remarkable sodium storage performance with high specific capacity, excellent cycle stability and good rate capability. This proposed strategy opens up a new path to design high-performance electrode materials for the storage of alkali metal ions.

1 Experimental Section

1.1 Synthesis of Graphite Oxide

In this study, the analytical grade of all chemical reactants was used. The graphite oxide (GO) was first prepared via the modified Hummer's method as previously presented by our group[31-32].

1.2 Synthesis of the Spherical Precursor

To synthetize the precursor, 0.1 mmol of $Ni(CH_3COO)_2\cdot 4H_2O$, 0.2 mmol of $Mn(CH_3COO)_2\cdot 4H_2O$, and 10 mL of glycerol were firstly dissolved into 30 mL of isopropanol to form a transparent brown solution. Secondly, the brown solution was then transferred into a Teflon-lined stainless steel autoclave and kept at 180 °C for 6 h. Finally, the brown precipitate was collected by centrifugation, cleaned thoroughly with ethanol and dried in an oven at 60 °C.

1.3 Synthesis of the Hollow Spheres $NiMn_2O_4$ and the R-NMN

For the fabrication of hollow spheres $NiMn_2O_4$, the as-synthesized precursor was annealed at 350 °C in air for 4 h with a slow heating rate of 2 $°C\cdot min^{-1}$.

In order to obtain the R-NMN, GO was dispersed in ethylene glycol by ultrasonic cell disruption for 30 min to form a 2.0 g·L^{-1} brown solution (denoted as Solution A). Subsequently, 30 mg precursor and 2.5 mL Solution A were added into 30 mL isopropanol under magnetic stirring at room temperature. The acquired solution was then transferred to a Teflon-lined stainless steel autoclave and kept at 180 °C for 6 h. After that, the black precipitate was gathered by washed with ethanol and dried in an oven at 60 °C. Finally, the target product (denoted as R-NMN-I containing 15 wt% rGO) was obtained through the heat treatment of dry precipitate at 350 °C for 4 h in Ar. For comparison, 5 mL and 7.5 mL Solution As were used in the above-mentioned experimental system without altering other reaction conditions for preparing R-NMN-II (25wt% rGO) and R-NMN-III(35 wt% rGO), respectively.

1.4 Materials Characterizations

The X-ray diffraction (XRD, D8 Advance of Bruker, Germany) with Cu-K_α radiation was used to investigate the crystallinity phases of samples. TGA curve of the spherical precursor was tested by Thermogravimetric analyzer (TGA, Pyris Diamond 6000 TG/DTA, American). The scanning electron microscope (SEM SU8010, Hitachi) coupled with energy dispersive spectroscope (EDS), transmission electron microscope (TEM JEOL JEM-3000F) were used for characterizing the morphologies of samples. The elemental information of the obtained materials was collected on X-ray photoelectron spectroscope (XPS, VG ESCALAB MK II).

1.5 Electrochemical Measurements

For the working electrode, 70wt% active material (the $NiMn_2O_4$, the R-NMN), 20wt% acetylene black, and 10wt% carboxyl methyl cellulose were first dispersed in N-methyl pyrrolidinone solvent to form a homogeneous slurry, and then spread onto a Cu foil. The working electrodes were dried overnight in an oven at 80 °C. The 2032 typed coin cells were assembled in an Ar-filled dry glovebox using metal sodium pieces as counter electrodes, glass fiber as the separator, and 1 mol·L^{-1} of $NaClO_4$ in ethylene carbonate and dimethyl carbonate (1:1 by volume) with 5wt% of fluoroethylene carbonate as the electrolyte. The Land battery testing system (LANHE CT2001A) was used for galvanostatic charge/discharge tests with various current densities in the voltage range of 0.01 ~ 3.0 V (vs. Na^+/Na). Cyclic voltammogram (CV) measurements were made with Princeton Applied Research VersaSTAT4 in the potential range of 0.01 ~ 3.00 V (vs. Na^+/Na) at a scan rate of 0.1 mV·s^{-1}. The frequency range from 0.01 Hz to 100 kHz was employed to measure electrochemical impedance spectrum (EIS) at an amplitude of 5 mV.

2 Results and Discussion

Fig. 1A shows XRD patterns of the as-prepared materials. Clearly, all the diffraction peaks of the

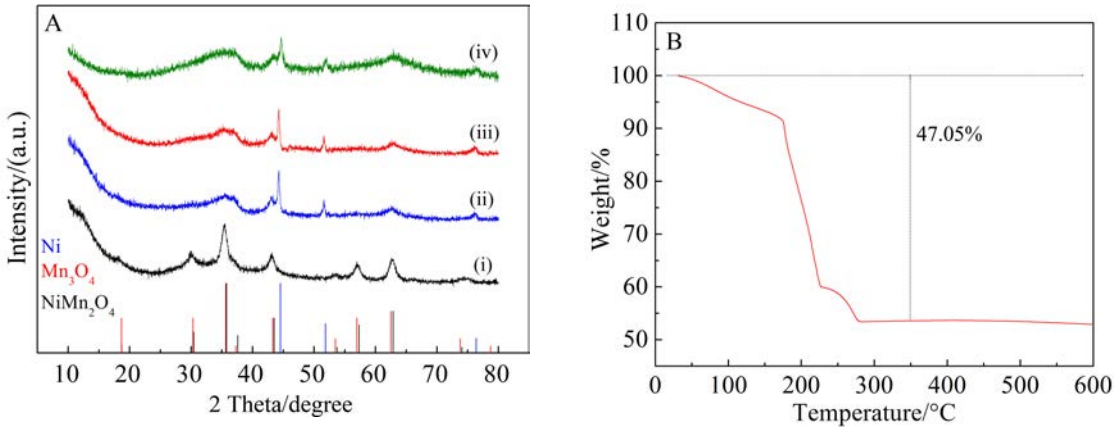

Fig. 1 (A) XRD patterns of (i) $NiMn_2O_4$, (ii) R-NMN-I, (iii) R-NMN-II and (iv) R-NMN-III; (B) TGA curve of the spherical precursor

pristine material can be indexed to the $NiMn_2O_4$ (JCPDS No.01-1110). Meanwhile, the additional diffraction peaks are observed in the R-NMN-I, R-NMN-II and R-NMN-III, which can be assigned to Mn_3O_4 (JCPDS No.13-0162) and Ni (JCPDS No.04-0850), derived from the reduction of rGO under annealing. A typical feature presented in XRD results is the broadening of diffraction peaks for R-NMN. Such a phenomenon can be ascribed to two aspects: (i) the coating of rGO reduces the crystallinity of products; (ii) the co-existence of pony-size Mn_3O_4 and $NiMn_2O_4$ leads to the broadening peak. TGA curve of the spherical precursor is shown in Fig. 1B. The different amounts of rGO contained in R-NMN were calculated from this curve.

To further verify the chemical structure, XPS measurement of R-NMN-II was carried out. Fig. 2 shows the high-resolution XPS spectra of Mn, Ni, C and O elements. As shown in Fig. 2A, two spin-orbit peaks at binding energies of 642.3 and 653.8 eV from the Mn 2p spectrum can be divided into four peaks. Two peaks centered at 642.8 eV and 653.6 eV are assigned to Mn $2p_{3/2}$ and Mn $2p_{1/2}$ of Mn^{3+}, respectively, while the other two peaks centered at 641.0 and 653.6 eV are attributed to Mn $2p_{3/2}$ and Mn $2p_{1/2}$ of Mn^{2+}, respectively[33]. Fig. 2B presents the Ni 2p spectrum. Two peaks at 854.6 and 872.0 eV are corresponding to Ni $2p_{3/2}$ and Ni $2p_{1/2}$, respectively. Simultaneously, two peaks located at 854.6 and 872.4 eV are assigned to Ni^{2+}, while the other peaks centered at 857 eV are attributed to Ni^{3+}[34]. As shown in the XPS spectrum of C_{1S} (Fig. 2C), two peaks located at 284.5 and 287.5 eV are related to C-C and O-C=O, respectively[34-35]. The XPS spectrum of O_{1S} in Fig. 2D can be separated into two peaks, which centered at 529.1 and 530.6 eV assigning to Ni-O-Mn and O-C=O/C=O isolated -OH, respectively[35-36]. From these observations, it can be confidently concluded that the nanocomposite consists of Mn_3O_4, $NiMn_2O_4$, Ni and conductive rGO, of which the rGO with few function-

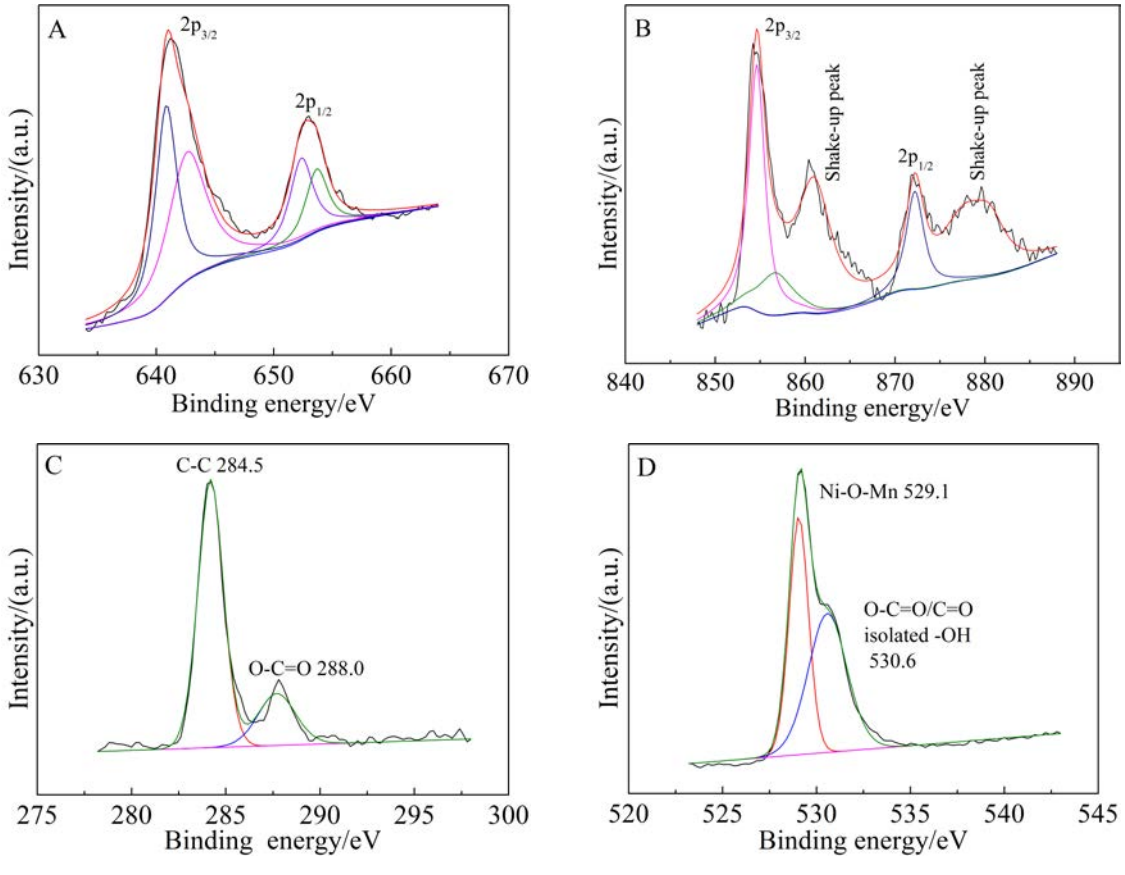

Fig. 2 XPS analyses of R-NMN-II: (A) Mn 2p, (B) Ni 2p, (C) C_{1s} and (D) O_{1s}

al groups possesses relatively high electronic conductivity.

The morphologies and structures of the desired materials were further confirmed by SEM and TEM. As shown in Fig. 3A, the morphology of $NiMn_2O_4$ is a type of uniformly spherical structure. High resolution image in Fig. 3B reveals that the diameter of sub-microsphere is approximately 250 nm. Meanwhile, the rough surface of $NiMn_2O_4$ indicates that the sub-microsphere consists of primary nanoparticles. As revealed by the TEM image in Fig. 3C, one can clearly observe the double-shelled hollow structure of secondary microspheres, and the core of microsphere is highly porous (Fig. 3D), resulting from the random stack of primary nanoparticles. Fig. 3E-G show the typical SEM and TEM images of the as-prepared R-NMN-II. Obviously, rGO encapsulated Ni/Mn_3O_4/$NiMn_2O_4$ constituting protective network would effectively promote the mechanical strength of nanocomposite (Fig. 3E and F). It should be noted here that the Ni/Mn_3O_4/$NiMn_2O_4$ microsphere is also the hollow construction with legible edge (Fig. 3G), which is identical to that of $NiMn_2O_4$. The HRTEM image (Fig. 3H) of R-NMN-II shows lattice fringes with spacing of 0.209 and 0.297 nm corresponding to the (400) and (220) planes of spinel $NiMn_2O_4$ (JCPDS No.01-1110) phase, respectively. Besides, the lattice distances of 0.203 and 0.243 nm correspond to the (100) and (222) crystal planes of Ni (JCPDS No.04-0850) and Mn_3O_4 (JCPDS No.13-0162), respectively. The corresponding EDS images shown in Fig. 4 also verify uniformly distributed Ni, Mn, O, and C in agreement with the XRD and XPS results.

The electrochemical properties of these as-prepared nanocomposites were investigated by cyclic voltammetry (CV) at a scan rate of 0.1 $mV \cdot s^{-1}$ in the potential window of 0.01 V to 3.0 V. Fig. 5A shows the first three CV curves of $NiMn_2O_4$. In the first cathodic process, the peak centered at 1.2 V is due to the reduction of Mn^{3+} to Mn^{2+}, and the peak centered at 0.55 V relates to the reduction of Mn^{2+} (Ni^{2+}) to Mn (Ni) and the formation of solid electrolyte interphase (SEI)[37-39]. In the anodic process, three oxidation peaks around 1.08 V, 1.54 V and 2.32 V are attributed to

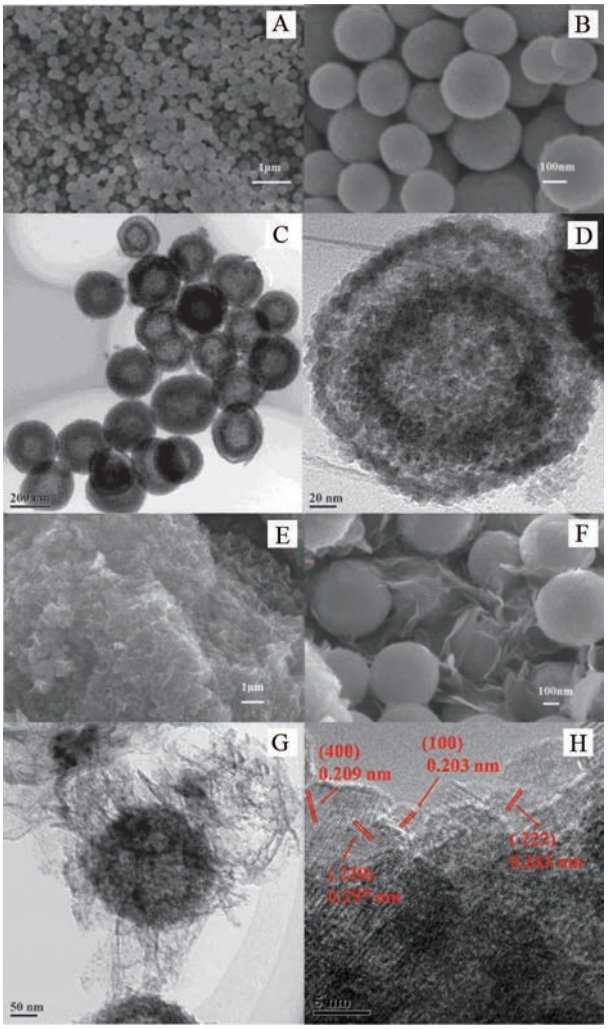

Fig. 3 (A, B) SEM and (E, F) TEM images of $NiMn_2O_4$; and (C, D) SEM and (G) TEM images of R-NMN-II; (H) HRTEM image of R-NMN-II.

the oxidations of Mn^0 to Mn^{2+} and Ni^0 to Ni^{2+}, and the decomposition of Na_2O matrix, respectively[37,40-41]. Owing to an irreversible transformation, the subsequent sweeps display an obvious difference comparing with the first one. Fig. 5B-D exhibit the CV curves of R-NMN-I, R-NMN-II, and R-NMN-III, which are similar to that of the pristine $NiMn_2O_4$. It should be noted here that the high peak specific currents achieved in R-NMN-I, R-NMN-II and R-NMN-III electrodes over the pristine one may suggest the improved electrochemical performance due to the presences of rGO and Ni metal.

Fig. 6A-B show the charge-discharge performances of the as-prepared nanocomposite for the 1st,

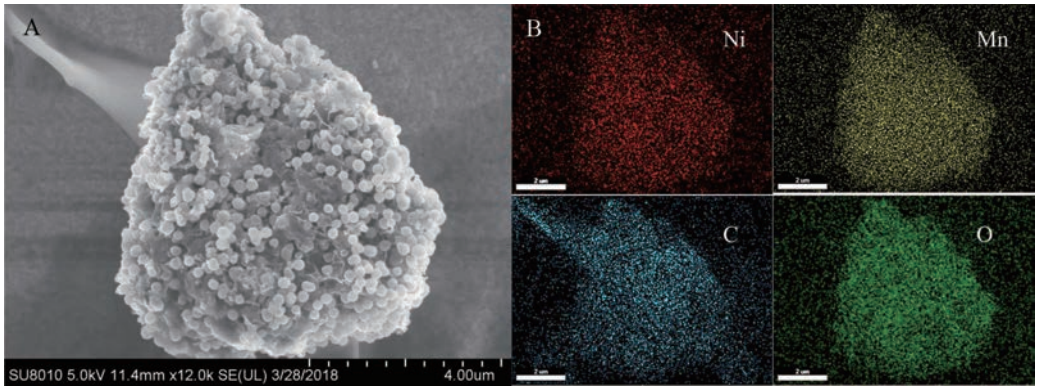

Fig. 4 (A) SEM image of R-NMN-II. The elemental mapping of (B) Ni, Mn, C, and O of R-NMN-II.

50th and 100th cycles at a current density of 50 mA·g^{-1} in the potential window of 0.01 ~ 3.0 V (vs. Na^+/Na). The first discharge/charge capacities of $NiMn_2O_4$ (Fig. 6A) and R-NMN-II (Fig. 6B) are 366.1/222.7 mAh·g^{-1} and 421.6/236.6 mAh·g^{-1}, respectively. Such a big irreversible capacity is mainly due to the formation of SEI film[41] matching well with CV results. The discharge/charge-capacities of $NiMn_2O_4$, R-NMN-II in the 100th cycle are 119.5/118.7 mAh·g^{-1} and 186.4/185.1 mAh·g^{-1}, respectively. Apparently, the R-NMN-II exhibits the superior electrochemical stability over the pristine one, which can be mainly attributed to the unique nanostructures and appropriate rGO content. Fig. 6C shows the cycling performances of $NiMn_2O_4$, R-NMN-I, R-NMN-II and R-NMN-III electrodes at a current density of 50 mA·g^{-1}. After 100 cycles, it is evident that the R-NMN-II delivers the best discharge capacity of 187.8 mAh·g^{-1} comparing with 126.3, 156.8 and 166.4 mAh·g^{-1} of $NiMn_2O_4$, R-NMN-I and R-NMN-III, respectively. The R-NMN electrodes

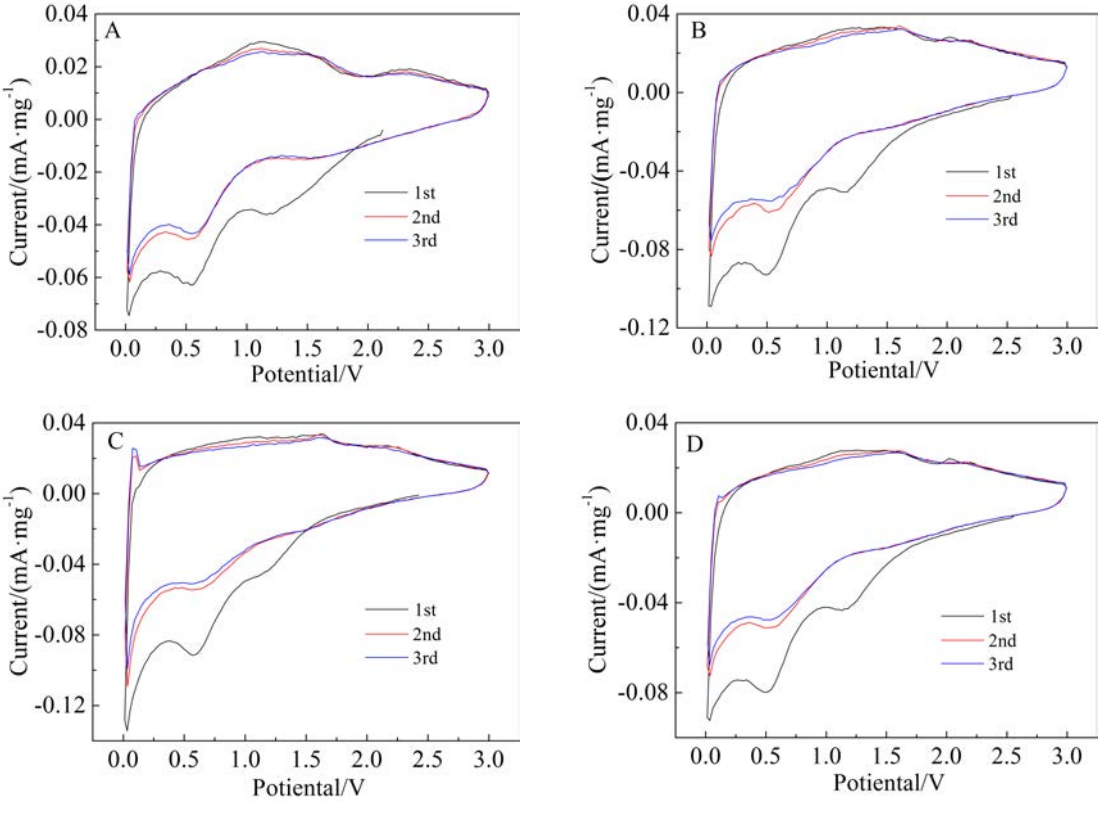

Fig. 5 CV curves of (A) $NiMn_2O_4$, (B) R-NMN-I, (C) R-NMN-II and (D) R-NMN-III in the 1st, 2nd and 3rd cycles.

show enhanced capacities compared with the $NiMn_2O_4$, which attributes to the following reasons: (i) the existences of rGO and Ni strengthen the electrical conductivity of the nanocomposite and also alleviate the volume expansion; (ii) the coexistence of Mn_3O_4 and $NiMn_2O_4$ can generate synergistic effects and enhance the electrochemical activity of sodium storage.

In order to compare the rate capabilities of the obtained materials, the as-prepared electrodes are evaluated at various current densities ranging from 50 to 800 $mA \cdot g^{-1}$, and the results are shown in Fig. 6D. Notably, the $NiMn_2O_4$ delivers poor discharge capacity of 65.6 $mAh \cdot g^{-1}$ at the current density 800 $mA \cdot g^{-1}$. In contrast, the R-NMN-I, R-NMN-II and R-NMN-III exhibit high specific capacities of 108.2, 150.3, and 127.2 $mAh \cdot g^{-1}$, respectively. It was obvious that R-NMN-II exhibits the highest discharge capacities of 234.3, 213.45, 192.9, 171.7 and 149.9 $mAh \cdot g^{-1}$ at the current densities of 50, 100, 200, 400, and 800 $mA \cdot g^{-1}$, respectively. When the current switches back to 50 $mA \cdot g^{-1}$, it is notabl that the R-NMN-II displays the high reversible capacity of 213.4 $mAh \cdot g^{-1}$ owing to its optimized composition and superior conductive network.

EIS measurements of the samples were employed to illustrate the change of electrode resistances in the electrochemical processes. As shown in Fig. 7, all the Nyquist plots of the samples consist of a partial semicircle at high frequency, a semicircle in medium frequency and an inclined line at low frequency. Thus, the equivalent circuit including R_s, R_{sf}, R_{ct}, CPE_{sf}, CPE_{ct} and W_s can be employed to fit the obtained data, as shown in the inset of Fig. 7. Ohmic resistance (R_s) is related to the resistances of electrolyte and electrode, and various contact resistances. The R_{sf} and CPE_{sf} are associated with surface SEI film connected with a partial semicircle at the high frequency. The R_{ct} and CPE_{ct} correspond to the charge transfer at interface between the electrode and elec-

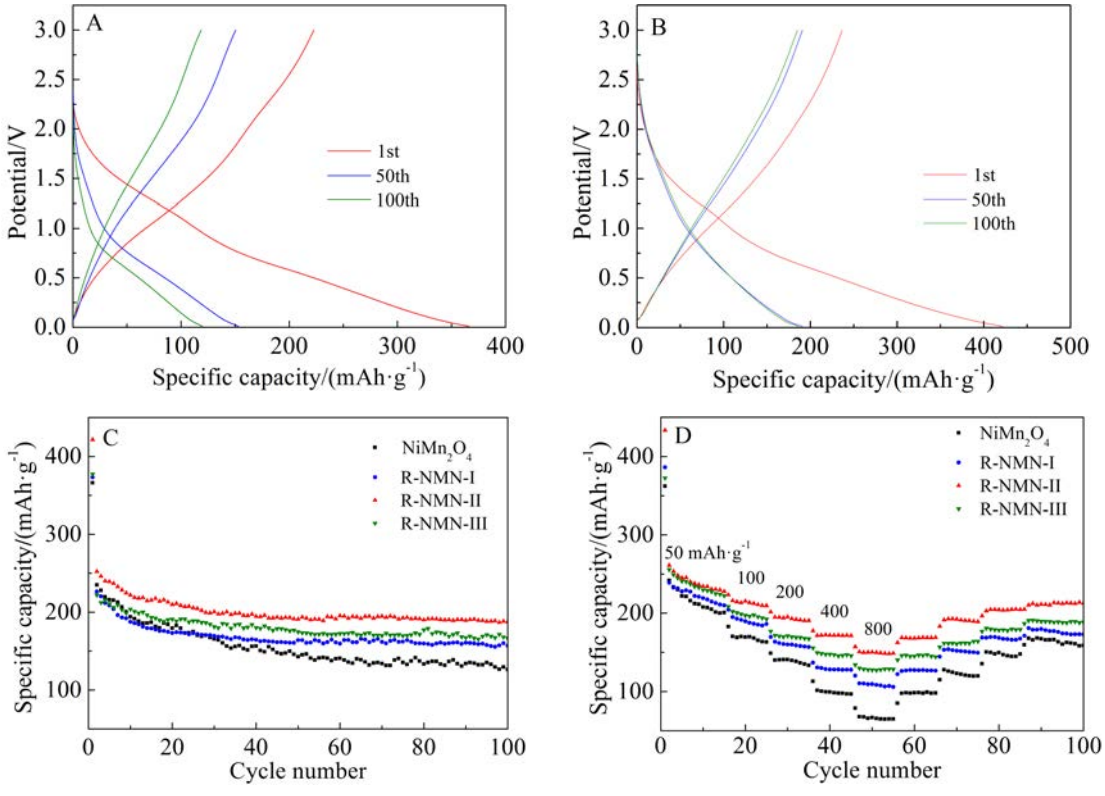

Fig. 6 The charge-discharge profiles of (A) $NiMn_2O_4$ and (B) R-NMN-II; (C) Cycling performances of $NiMn_2O_4$, R-NMN-I, R-NMN-II, and R-NMN-III; (D) Rate capability performances of $NiMn_2O_4$, R-NMN-I, R-NMN-II, and R-NMN-III at various current densities.

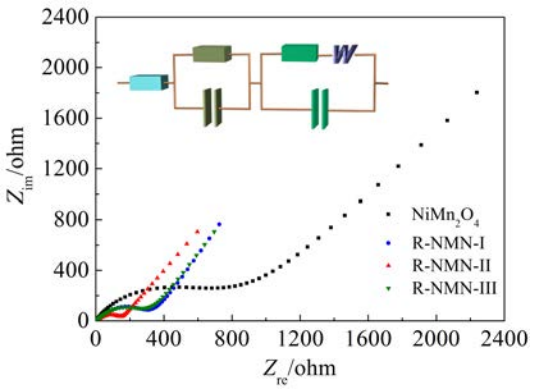

Fig. 7 Nyquist plots of $NiMn_2O_4$, R-NMN-I, R-NMN-II and R-NMN-III after 10 cycles. The inset shows the equivalent circuit.

trolyte, which are connected with the semicircle in medium frequency. W_s is related to the sodium ion diffusion in the bulk of electrode, which is consistent with the inclined line[40, 42-43]. It is clear that R_{ct} values of the R-NMN-I, R-NMN-II and R-NMN-III display much lower values (306.7 Ω, 151.2 Ω, 273.5 Ω, respectively) than that of $NiMn_2O_4$ (1179 Ω), further illustrating the superior cycling performance and rate capability of nanocomposite over that of the $NiMn_2O_4$.

3 Conclusions

The Ni/Mn_3O_4/$NiMn_2O_4$ coated with rGO was first synthesized via one-step solvothermal treatment followed by subsequent annealing. Benefiting from rGO, metal nickel and hollow structure, the R-NMN, served as an anode material for SIBs, delivers the enhanced rate performances and durable long-term cycling stability. In particular, the R-NMN-II exhibits the highest discharge capacity of 187.8 mAh·g^{-1} after 100 cycles at 50 mA·g^{-1}, and a high rate capacity of 149.9 mAh·g^{-1} achieved at 800 mA·g^{-1}. Such an obvious improvement in sodium storage is mainly attributed to the enhanced conductivity, reduced ion diffusion distance and suppressed volume fluctuation. Undoubtedly, our strategy is a promising research direction to develop alternative high-performance anode material for SIBs and beyond.

Acknowledgements

This research was supported by the National Natural Science Foundation of China (51572194), the national Key Research and Development Program of China (No. 2018YFB0105900), and the Tianjin Major Program of New Materials Science and Technology (No. 16ZXCLGX00070).

References:

[1] Bruce P G, Scrosati B, Tarascon J M. Nanomaterials for rechargeable lithium batteries[J]. Angewandte Chemie International Edition, 2008, 47(16): 2930-2946.

[2] Wu H B, Chen J S, Hng H H, et al. Nanostructured metal oxide-based materials as advanced anodes for lithium-ion batteries[J]. Nanoscale, 2012, 4(8): 2526-2542.

[3] Armand M, Tarascon J M. Building better batteries[J]. Nature, 2008, 451(7179): 652-657.

[4] Larcher D, Tarascon J M. Towards greener and more sustainable batteries for electrical energy storage[J]. Nature Chemistry, 2015, 7(1): 19-29.

[5] Scrosati B, Hassoun J, Sun Y K. Lithium-ion batteries. A look into the future[J]. Energy & Environmental Science, 2011, 4(9): 3287-3295.

[6] Stevens D A, Dahn J R. The mechanisms of lithium and sodium insertion in carbon materials[J]. Journal of The Electrochemical Society, 2001, 148(8): A803-A811.

[7] Hong S Y, Kim Y, Park Y, et al. Charge carriers in rechargeable batteries: Na ions vs. Li ions[J]. Energy & Environmental Science, 2013, 6(7): 2067-2081.

[8] Kundu D, Talaie E, Duffort V, et al. The emerging chemistry of sodium ion batteries for electrochemical energy storage[J]. Angewandte Chemie International Edition, 2015, 54(11): 3431-3448.

[9] Wang J Y, Yang N L, Tang H J, et al. Accurate control of multishelled Co_3O_4 hollow microspheres as high-performance anode materials in lithium-ion batteries[J]. Angewandte Chemie-International Edition, 2013, 52(25): 6417-6420.

[10] Ren S H, Zhao X G, Chen R Y, et al. A facile synthesis of encapsulated $CoFe_2O_4$ into carbon nanofibres and its application as conversion anodes for lithium ion batteries [J]. Journal of Power Sources, 2014, 260: 205-210.

[11] Sekhar B C, Packiyalakshmi P, Kalaiselvi N. Custom designed $ZnMn_2O_4$/nitrogen doped graphene composite anode validated for sodium ion battery application[J]. RSC Advances, 2017, 7(32): 20057-20061.

[12] Yuan C Z, Wu H B, Xie Y, et al. Mixed transition-metal oxides: design, synthesis, and energy-related applications [J]. Angewandte Chemie International Edition, 2014, 53 (6): 1488-1504.

[13] Zhang W M, Cao P, Li L, et al. Carbon-encapsulated 1D SnO_2/NiO heterojunction hollow nanotubes as high-per-

formance anodes for sodium-ion batteries[J]. Chemical Engineering Journal, 2018, 348: 599-607.

[14] Shen L, Yu L, Yu X Y, et al. Self-templated formation of uniform $NiCo_2O_4$ hollow spheres with complex interior structures for lithium-ion batteries and supercapacitors[J]. Angewandte Chemie International Edition, 2015, 54(6): 1868-1872.

[15] Yuan S(袁双), Zhu Y H(朱云海), Wang S(王赛), et al. Micro/nano-structured electrode materials for sodium-ion batteries[J]. Journal of Electrochemistry(电化学), 2016, 22(5): 464-476.

[16] Zhou W(周文), Lu X F(卢雪峰), Wu M M(吴明娲), et al. Template-assisted hydrothermal synthesis of NiO@Co_3O_4 hollow spheres with hierarchical porous surfaces for supercapacitor applications[J]. Journal of Electrochemistry(电化学), 2016, 22(5): 513-520.

[17] Duan S Y(段舒怡), Zhang W(张伟), Piao J Y(朴俊宇), et al. Uniform nanoshells for functional materials: Constructions and applications[J]. Journal of Electrochemistry (电化学), 2016, 22(3): 260-270.

[18] Chen J F, Ru Q, Mo Y D, et al. Design and synthesis of hollow $NiCo_2O_4$ nanoboxes as anode for lithium-ion and sodium-ion batteries[J]. Physical Chemistry Chemical Physics, 2016, 18(28): 18949-18957.

[19] Choi J S, Lee H J, Ha J K, et al. Synthesis and electrochemical properties of amorphous carbon coated Sn anode material for lithium ion batteries and sodium ion batteries[J]. Journal of Nanoscience and Nanotechnology, 2018, 18(9): 6459-6462.

[20] Che Q, Zhang F, Zhang X G, et al. Preparation of ordered mesoporous carbon/$NiCo_2O_4$ electrode and its electrochemical capacitive behavior[J]. Acta Physico-Chimica Sinica, 2012, 28(4): 837-842.

[21] Zhou D, Li X, Fan L Z, et al. Three-dimensional porous graphene-encapsulated CNT@SnO_2 composite for high-performance lithium and sodium storage[J]. Electrochimica Acta, 2017, 230: 212-221.

[22] Zhang R F, Wang Y K, Zhou H, et al. Mesoporous TiO_2 nanosheets anchored on graphene for ultra long life Na-ion batteries[J]. Nanotechnology, 2018, 29(22): 225401.

[23] Jiang H(江恒), Fan J M(范镜敏), Zheng M S(郑明森), et al. $Co_3(HCOO)_6$@rGO as a promising anode for lithium ion batteries[J]. Journal of Electrochemistry(电化学), 2018, 24(3): 207-215.

[24] Cai D P, Qu B H, Li Q H, et al. Reduced graphene oxide uniformly anchored with ultrafine $CoMn_2O_4$ nanoparticles as advance anode materials for lithium and sodium storage[J]. Journal of Alloys and Compounds, 2017, 716: 30-36.

[25] Zou F, Chen Y M, Liu K W, et al. Metal organic frameworks derived hierarchical hollow NiO/Ni/graphene composites for lithium and sodium storage[J]. ACS Nano, 2016, 10(1): 377-386.

[26] Zeng L Z, Zhang W G, Xia P, et al. Porous $Ni_{0.1}Mn_{0.9}O_{1.45}$ microellipsoids as high-performance anode electrocatalyst for microbial fuel cells[J]. Biosensors and Bioelectronics, 2018, 102: 351-356.

[27] Ren M M, Li F Y, Xu H, et al. CoO/$CoFe_2O_4$ bi-component nanorod core with S-doped carbon shell as excellent anode for lithium ion battery[J]. Journal of Alloys and Compounds, 2018, 737: 442-447.

[28] Huang G, Zhang F F, Zhang L L, et al. Hierarchical $NiFe_2O_4$/Fe_2O_3 nanotubes derived from metal organic frameworks for superior lithium ion battery anodes[J]. Journal of Materials Chemistry A, 2014, 2(21): 8048-8053.

[29] Ma Y, Ma Y J, Geiger D, et al. ZnO/$ZnFe_2O_4$/N-doped C micro-polyhedrons with hierarchical hollow structure as high-performance anodes for lithium-ion batteries[J]. Nano Energy, 2017, 42: 341-352.

[30] Xu J M, He L, Wang Y J, et al. Preparation of bi-component ZnO/$ZnCo_2O_4$ nanocomposites with improved electrochemical performance as anode materials for lithium-ion batteries[J]. Electrochimica Acta, 2016, 191: 417-425.

[31] Hummers Jr W S, Offeman R E. Preparation of graphitic oxide[J]. Journal of the American Chemical Society, 1958, 80(6): 1339-1339.

[32] Shan H, Xiong D B, Li X F, et al. Tailored lithium storage performance of graphene aerogel anodes with controlled surface defects for lithium-ion batteries[J]. Applied Surface Science, 2016, 364: 651-659.

[33] Li J F, Xiong S L, Li X W, et al. A facile route to synthesize multiporous $MnCo_2O_4$ and $CoMn_2O_4$ spinel quasi-hollow spheres with improved lithium storage properties [J]. Nanoscale, 2013, 5(5): 2045-2054.

[34] Huang J R, Wang W, Lin X R, et al. Three-dimensional sandwich-structured $NiMn_2O_4$@reduced graphene oxide nanocomposites for highly reversible Li-ion battery anodes[J]. Journal of Power Sources, 2018, 378: 677-684.

[35] Yu Z X, Li X F, Yan B, et al. Rational design of flower-like tin sulfide@ reduced graphene oxide for high performance sodium ion batteries[J]. Materials Research Bulletin, 2017, 96: 516-523.

[36] Maiti S, Pramanik A, Dhawa T, et al. Bi-metal organic framework derived nickel manganese oxide spinel for lithium-ion battery anode[J]. Materials Science and Engi-

neering B - Advanced Functional Solid-State Materials, 2018, 229: 27-36.

[37] Li F, Ma J Y, Ren H J, et al. Fabrication of MnO nanowires implanted in graphene as an advanced anode material for sodium-ion batteries[J]. Materials Letters, 2017, 206: 132-135.

[38] Chang L, Wang K, Huang L G, et al. Hierarchically porous $CoNiO_2$ nanosheet array films with superior sodium storage performance[J]. New Journal of Chemistry, 2017, 41 (23): 14072-14075.

[39] Sekhar B C, Packiyalakshmi P, Kalaiselvi N. Custom designed $ZnMn_2O_4$/nitrogen doped graphene composite anode validated for sodium ion battery application[J]. RSC Advances, 2017, 7(32): 20057-20061.

[40] Kou H R, Li X F, Shan H, et al. An optimized Al_2O_3 layer for enhancing the anode performance of $NiCo_2O_4$ nanosheets for sodium-ion batteries[J]. Journal of Materials Chemistry A, 2017, 5(34): 17881-17888.

[41] Wu X H, Wu W W, Wang K T, et al. Synthesis and electrochemical performance of flower-like $MnCo_2O_4$ as an anode material for sodium ion batteries[J]. Materials Letters, 2015, 147: 85-87.

[42] Wu Z Y, Li X F, Tai L M, et al. Novel synthesis of tin oxide/graphene aerogel nanocomposites as anode materials for lithium ion batteries[J]. Journal of Alloys and Compounds, 2015, 646: 1009-1014.

[43] Yang M, Li X F, Yan B, et al. Reduced graphene oxide decorated porous SnO_2 nanotubes with enhanced sodium storage[J]. Journal of Alloys and Compounds, 2017, 710: 323-330.

Ni/Mn_3O_4/$NiMn_2O_4$@RGO 空心微球负极的制备及其储钠性能

颜　冲[1],寇华日[2],颜　波[2],刘晓静[1],李德军[1],李喜飞[1,2*]

(1. 天津师范大学物理与材料科学学院,天津市储能材料表面技术国际联合研究中心,天津 300387;
2. 西安理工大学先进电化学能源研究院 & 材料科学与工程学院,陕西 西安 710048)

摘要:采用溶剂热法制备前驱体,后经 350 °C 热处理,首次合成了空心结构的 $NiMn_2O_4$ 微球以及不同含量氧化石墨烯包覆的 Ni/Mn_3O_4/$NiMn_2O_4$@RGO 复合材料. 电化学性能测试表明,复合负极材料中,含 25wt%还原氧化石墨烯的材料储钠性能最佳,其在 50 mA·g^{-1} 电流密度下,100 次循环后放电比容量保持在 187.8 mAh·g^{-1},且 800 mA·g^{-1} 电流密度下的可逆容量高达 149.9 mAh·g^{-1},明显优于 $NiMn_2O_4$ 及其他石墨烯基复合材料. 研究指出,复合材料性能的提升得益于空心微球和还原的氧化石墨烯构成的特殊结构,一方面缩短了电子/离子传输距离,缓解了体积效应,另一方面高导电网络有效增强了活性物质利用率.

关键词: Ni/Mn_3O_4/$NiMn_2O_4$;还原氧化石墨烯;负极材料;钠离子电池